Supporting Information

Wang et al. 10.1073/pnas.1203952109

SI Materials and Methods

Histochemical and Immunofluorescence Analysis. For histological and immunofluorescence studies, bladders were processed as described (1). The following primary antibodies were used: (*i*) rabbit and goat polyclonal antibodies to *E. coli* (United States Biological), (*ii*) mouse monoclonal antibody to E-cadherin (BD Bioscience), (*iii*) goat polyclonal antibodies to BrdU, (*iv*) rat monoclonal antibody to Lamp1 (clone ID4B; Developmental Hybridoma Bank, National Institute of Child Health and Human Development), (*v*) rabbit polyclonal to LC3B (Novus), (*vi*) guinea pig polyclonal to p62 (Progen), and (*vii*) rabbit polyclonal to Atg16L1 (Abgent). Antigen–antibody complexes were detected with Alexa Fluor 488-, 594-, and 647-conjugated secondary antibodies (Invitrogen). Images were obtained using Zeiss Apotome at 10–20× and 40–63× (oil) magnifications.

Immunoblotting Analysis. Bladders were isolated, processed, and immunoblotted using primary antibodies (2) [(*i*) rabbit polyclonal to Atg16L1 (Abgent), (*ii*) goat polyclonal to UP1a (Santa Cruz), and (*iii*) rabbit monoclonal to GAPDH (Cell Signaling)] and secondary antibodies [(*i*) goat anti-rabbit IgGHRP and (*ii*) donkey anti-goat IgG-HRP (Santa Cruz)]. The protein bands on the developed film were quantified by Image J (http://rsb.info.nih.gov/ij/).

BrdU Labeling. BrdU labeling was performed as described (1).

Quantitative Real-Time PCR Analysis. RNA was isolated from bladders from uninfected and infected (6 hpi) animals ($n = 3$ mice per genotype) and processed as described (1).

The following primers were used for detection of the targets (forward primers are listed first followed by reverse primers): 18s, 5′-CGGCTACCACATCCAAGGAA-3′ and 5′-GCTGGAATTACCGCGGCT-3′; IL-1β, 5′-GCAACTGTTCCTGAACTCAACT-3′ and 5′-ATCTTTTGGGGTCCGTCAACT-3′; IL-18, 5′-GACTCTTGCGTCAACTTCAAGG-3′ and 5′-CAGGCTGTCTTTTGTCAACGA-3′; IL-6, 5′-CCAGAAACCGCTATGAAGTTCCT-3′ and 5′-CACCAGCATCAGTCCCAAGA-3′; IL-1α, 5′-GCACCTTACACCTACCAGAGT-3′ and 5′-AAACTTCTGCCTGACGAGCTT-3′; KC, 5′-ACCCAAACCGAAGTCATAGCC-3′ and 5′-TTCAGGGTCAAGGCAAGCC-3′; and MIP-2, 5′-TGAGTGTGACGCCCCCA-3′ and 5′-TTTTTGACCGCCCTTGAGAG-3′.

1. Mysorekar IU, Isaacson-Schmid M, Walker JN, Mills JC, Hultgren SJ (2009) Bone morphogenetic protein 4 signaling regulates epithelial renewal in the urinary tract in response to uropathogenic infection. *Cell Host Microbe* 5:463–475.

2. Cadwell K, et al. (2008) A key role for autophagy and the autophagy gene Atg16l1 in mouse and human intestinal Paneth cells. *Nature* 456:259–263.

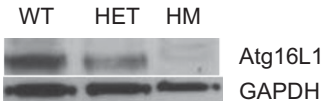

Fig. S1. Expression of Atg16L1 protein in Atg16L1^{HM} (HM) bladders. HM and Atg16L1^{HM} heterozygote mice (only one hypomorphic allele) mice show 78% and 59% knockdown of the Atg16L1 protein, respectively (~68-kDa doublet) compared with WT. Knockdown was measured by immunoblotting and normalized to GAPDH loading control. $n = 2$ experiments.

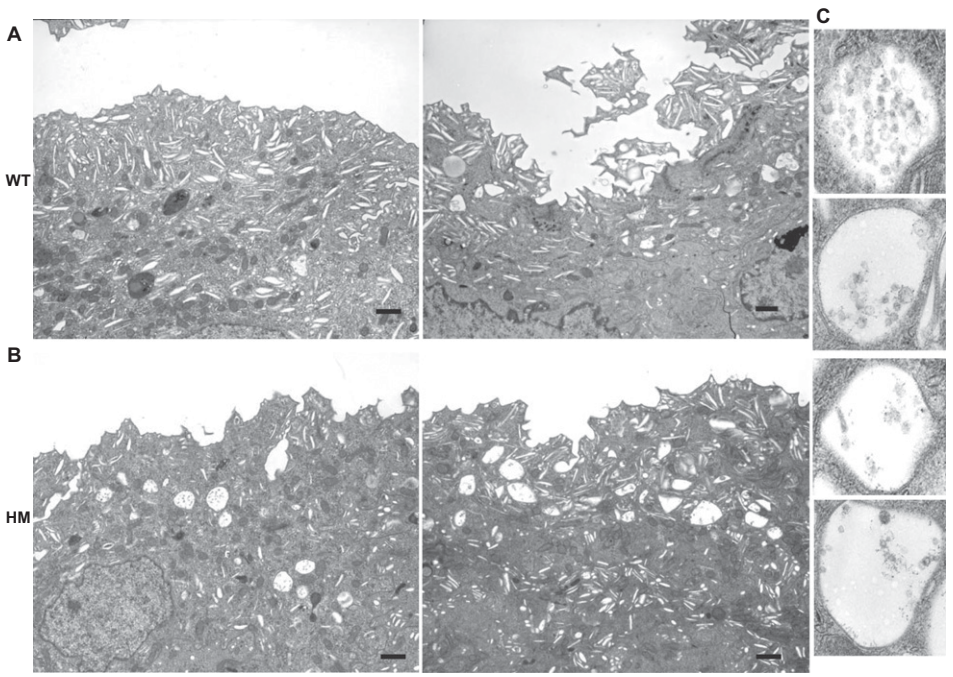

Fig. S2. Atg16L1 deficiency is associated with superficial cell ultrastructural abnormalities. (*A* and *B*) Transmission EM showing WT (*A*) and HM (*B*) superficial cell ultrastructure depicting architectural changes in HM urothelium. (Scale bar: 1 μm.) (*C*) High magnification images showing multivesicular bodies (MVBs) from HM superficial cells.

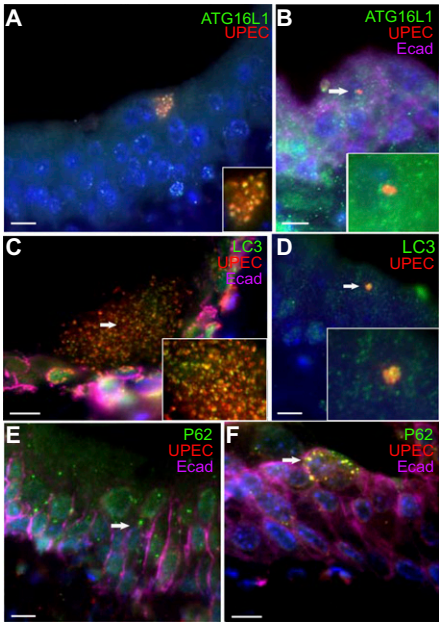

Fig. S3. Intracellular uropathogenic *Escherichia coli* (UPEC) colocalizes with autophagic machinery. (*A* and *B*) Atg16L1 colocalizes with UPEC (red) within an intracellular bacterial community at 6 h postinoculation (hpi; *A* and *A Inset*) and a quiescent intracellular reservoir at 14 d postinoculation (dpi; *B*, arrow and *B Inset*). (*C* and *D*) Light chain 3 puncta (green) colocalize with UPEC (red) within an intracellular bacterial community at 6 hpi (*C* and *C Inset*) and a quiescent intracellular reservoirs at 14 dpi (*D*, arrow and *D Inset*). (*E*) p62 puncta (green, arrow) in uninfected bladders occur diffusely throughout the urothelium. (*F*) On UPEC infection (6 hpi), p62 puncta (green) colocalize with invaded UPEC (red, arrow). n = 5–10 mice per time point per genotype, and n = 3 experiments. (Scale bar: 10 μm.)

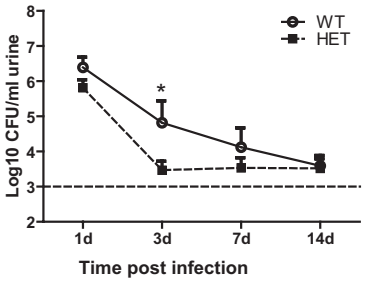

Fig. S4. A single hypomorphic *Atg16L1* allele is sufficient to confer protection to UPEC infection. CFU counts of bacteriuria plotted as mean ± SEM of the log10 value 1–14 dpi, indicating significant reductions of bacteriuria in Atg16L1 heterozygote mice at 3 dpi. n = 5–15 mice per time point per genotype; n = 2 experiments. *$P < 0.05$ by two-way ANOVA with Bonferroni posttest.

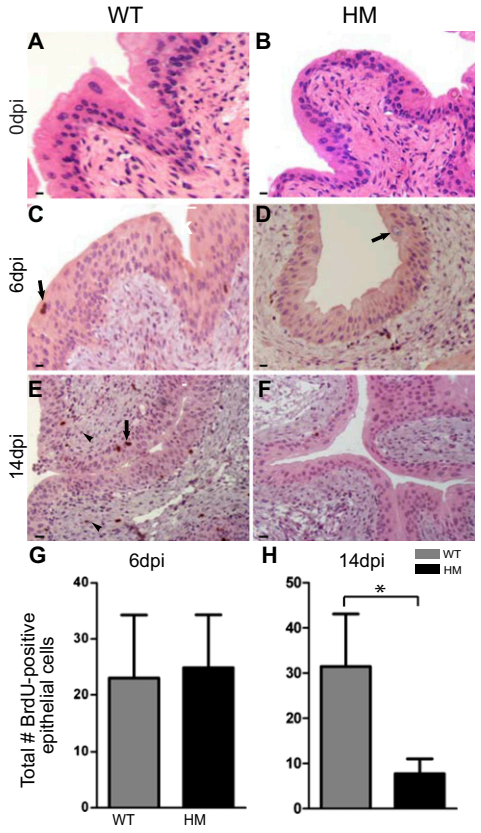

Fig. S5. Superficial urothelial cell regeneration postinfection is hastened in Atg16L1-deficient bladders. (*A* and *B*) H&E- and BrdU-stained WT (*A*) and HM (*B*) bladders at 0 dpi, respectively, showing normal morphology of the bladder before infection with no BrdU$^+$ cells observed. (*C*–*F*) H&E- and BrdU-stained WT (*C* and *E*) and HM (*D* and *F*) bladders at 6 and 14 dpi, showing BrdU$^+$ cells (brown, arrows in *C* and *E*), neutrophils (*C* and *E*, arrowhead), and superficial cells (arrow in *D*). (Scale bar: 10 μm.) BrdU counts at (*G*) 6 and (*H*) 14 dpi depicting rapid recovery from infection in HM mice. n = 15–20 mice per time point per condition. Bars represent mean ± SEM. *$P < 0.05$ by unpaired two-tailed t test.

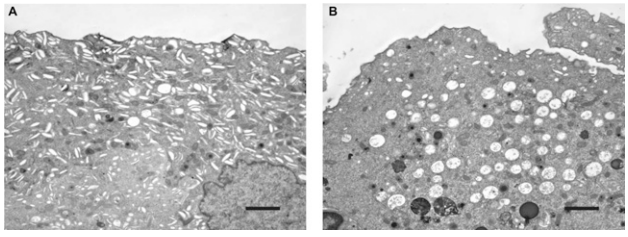

Fig. S6. Atg16L1 deficiency-induced alteration of superficial cell architecture is intrinsic to the deficiency and not altered by infection. Transmission EM analysis showing WT (*A*) and HM (*B*) newly regenerated superficial cells at 14 dpi, depicting ultrastructural abnormalities in HM urothelium. (Scale bar: 2 μm.)

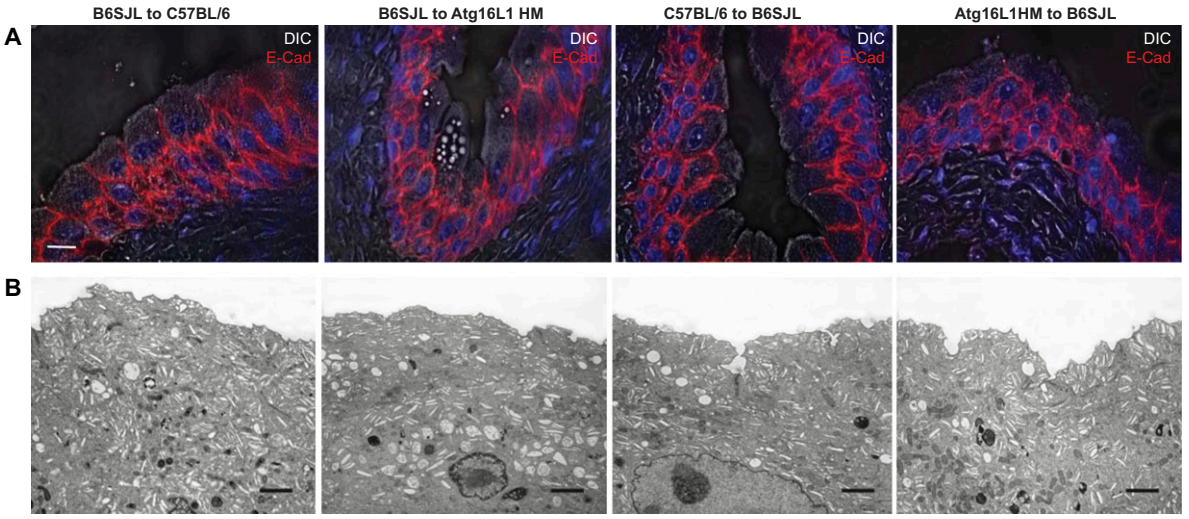

Fig. S7. Atg16L1 deficiency in the hematopoietic compartment does not induce epithelial abnormalities. (*A*) Immunofluorescence (IF) and differential interference contrast (DIC) imaging analysis showing enhanced vesicular congestion in Atg16L1^{HM} recipients receiving WT bone marrow but not in WT mice receiving HM bone marrow. E-cadherin (red) outlines urothelial cells; nuclei are blue with biz-benzimide. (Scale bar: 10 μm.) (*B*) Transmission EM showing superficial cell ultrastructures in different groups of mice, confirming the presence of architectural defects in Atg16L1^{HM} recipients receiving WT bone marrow urothelium. (Scale bar: 1 μm.)

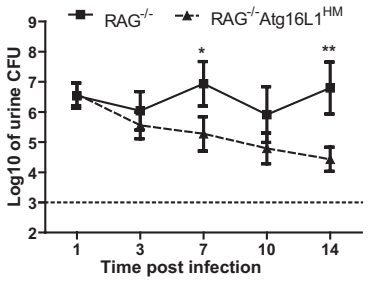

Fig. S8. Atg16L1 deficiency in the innate immune compartment induces enhanced bacteriuric clearance in mice lacking an intact adaptive immune system. Rag1$^{-/-}$/Atg16L1^{HM} double mutants on a C57BL/6 strain background were generated by first back-crossing Atg16L1^{HM} mice onto a C57BL/6 background and then breeding with Rag1$^{-/-}$ mice. CFU counts of bacteriuria plotted as mean ± SEM of the log10 value 1–14 dpi indicating significant reduction in bacteriuria in Rag1$^{-/-}$/Atg16L1^{HM} mice at 7–14 dpi compared with Rag1$^{-/-}$ mice. n = 5–15 mice per time point per genotype; n = 2 experiments. *$P < 0.05$, **$P < 0.01$ by two-way ANOVA with Bonferroni posttest.

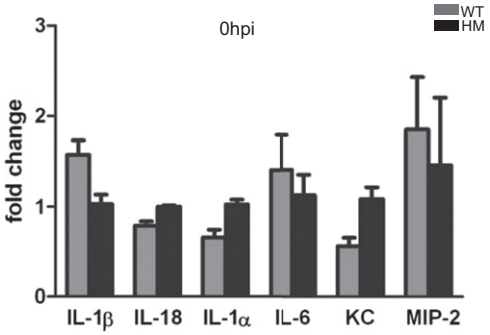

Fig. S9. Atg16L1 deficiency does not induce alterations in overall cytokine profiles before UPEC infection. Quantitative RT-PCR analysis of bladder tissue cytokine mRNA levels in uninfected WT and HM bladders does not exhibit any differences at baseline. Bars represent mean ± SEM; n = 3 mice/genotype.

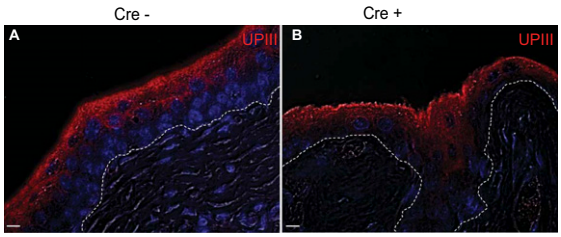

Fig. S10. Atg5 deficiency in macrophages and granulocytes does not exhibit altered urothelial architecture. IF and DIC imaging analysis showing $Atg5^{fl/fl}$-Lyz-Cre^{-} (*A*) and Cre^{+} (*B*) bladder superficial cells with normal uroplakin III (red) staining and no organellar congestion. (Scale bar: 10 μm.)